Article:

Murasovs, N., Lloyd, P., Bacchetti, A. et al. (7 more authors) (Accepted: 2025) Gradient Pulling of a Tethered Robot via a Magnetic Resonance Imaging System. Device. ISSN 2666-9986 (In Press)

Gradient Pulling of a Tethered Robot via a Magnetic Resonance Imaging System

Nikita Murasovs[1,5,*], Peter Lloyd[1], Alistair Bacchetti[1], Yael L. May[1], Joshua Armitage[2], Oscar Cespedes[3], Erica Dall'Armellina[4], James H. Chandler[1], Jürgen E. Schneider[4,**], and Pietro Valdastri[1,***]

[1]Department of Electrical and Electronic Engineering, University of Leeds, Leeds LS2 9JT, UK
[2]Department of Mechanical Engineering, University of Leeds, Leeds LS2 9JT, UK
[3]Department of Physics and Astronomy, University of Leeds, Leeds LS2 9JT, UK
[4]Leeds Institute of Cardiovascular and Metabolic Medicine, University of Leeds, Leeds LS2 9JT, UK
[5]Lead contact
[*]Correspondence: elnmur@leeds.ac.uk
[**]Correspondence: j.e.schneider@leeds.ac.uk
[***]Correspondence: p.valdastri@leeds.ac.uk

SUMMARY

Magnetically actuated soft robots offer significant advantages for minimally invasive medical procedures by enabling precise control and navigation in confined anatomical environments. This study explores the feasibility of using the gradient fields of a Magnetic Resonance Imaging (MRI) system to actuate a tethered robotic guidewire, demonstrating a novel leader-follower approach for controlled navigation. A spherical low-carbon steel ball, tethered via a medical-grade filament, serves as the actuated magnetic tip, while a flexible silicone sleeve follows the tip trajectory to establish a stable guidewire. By leveraging the MRI's built-in magnetic gradients, we achieve stepwise actuation and thus pathway formation inside the MRI bore. We analyze the magnetic pulling force, the friction effects of the tether and sleeve combination, and the signal void introduced by the presence of ferrous materials in the MRI bore, optimizing the system to minimize imaging distortion while maintaining effective actuation. Experimental results demonstrate successful free space deformation and gradient-induced forward movement followed by follower navigation through constrained pathways, validating the method's potential for MRI-guided endovascular interventions.

KEYWORDS

magnetic resonance imaging, soft robotics, robotic guidewire, leader-follower navigation

INTRODUCTION

In recent years, soft robotics has advanced considerably, offering safer and more adaptable tools for minimally invasive medical procedures. Unlike conventional rigid robotic systems, soft robots are composed of highly compliant and deformable materials that can conform to the body's complex anatomy. This inherent flexibility makes them especially suitable for delicate operations in confined anatomical regions such as blood vessels, pulmonary airways, and the gastrointestinal tract[1,2]. By conforming more effectively to biological tissues, soft robotic systems have the potential to overcome limitations of traditional rigid endoscopic and catheter-based instruments, thereby minimizing the risk of tissue injury during navigation[3].

One particularly promising area within soft robotics involves magnetic actuation for medical applications. These robots are manipulated using external magnetic fields, eliminating the need for physical connections such as cables or tubing. This remote actuation method supports the development of highly miniaturized robots—down to millimeter or even sub-millimeter dimensions—enabling less invasive procedures and access to anatomically challenging regions[4]. Recent research demonstrates that magnetically actuated soft robots can perform intricate tasks in tight spaces, including targeted drug delivery, tissue sampling, and obstruction removal[5].

Despite these advantages, the widespread clinical adoption of magnetic soft medical robots is hindered by challenges in achieving precise control and reliable feedback. Real-world operation demands advanced sensing and actuation systems capable of enabling accurate navigation and manipulation, particularly at small scales. Magnetic Resonance Imaging (MRI), a widely used clinical imaging technology, offers a compelling solution. Beyond providing high-resolution, real-time, 3D imaging without ionizing radiation, MRI systems can potentially be used to actuate magnetic robots through their built-in magnetic fields and gradients. This integrated approach could facilitate simultaneous visualization and control, a breakthrough capability for the field of medical robotics[6].

Achieving closed-loop control requires accurate localization and shape estimation, especially in visually occluded or cluttered environments. Several techniques have been explored to address this, including fiber optic strain sensors, ultrasound imaging, infrared systems[7], and fluoroscopy. However, each comes with drawbacks: fiber optics can stiffen the robot[8], ultrasound data is often noisy and incomplete[9], and fluoroscopy, though effective, is limited to 2D imaging and involves ionizing radiation, making it unsuitable for frequent use[10–13]. MRI stands out as a potentially ideal platform for both tracking and actuation, leveraging existing infrastructure to estimate a robot's position and shape in real time[6]. Nevertheless, the presence of magnetic materials interferes with imaging, leading to artifacts, distortions, and signal loss, which complicates the concurrent use of MRI for both imaging and actuation[14].

[R1.1] Over the past two decades, extensive research efforts have focused on leveraging MRI systems for controlled robotic surgeries. Three primary MRI-driven actuation methods have been explored: magnetic gradient pulling using gradient coils[15–17], magnetic gradient pulling based on magnet-to-magnet interactions[18,19], and Lorentz force-based actuation[20,21]. Various system designs and clinical applications have also been developed, including magnetic bead-based catheter navigation[22–24], MRI-driven hammer robots for tissue penetration[25], and capsule robots for drug delivery[26,27]**[R2.2]**. Tethered medical robot designs reported in the literature generally fall into two main actuation categories: Lorentz torque and gradient pulling. Lorentz torque approaches, typically implemented through solenoid coil designs[20,21], utilize cables to deliver power and generate localized magnetization, offering enhanced control through additional degrees of freedom (DOF). However, these systems are limited by complex cable arrangements, challenges in device miniaturization, and relatively low force generation[6]. In contrast, gradient pulling-based designs, which often employ a magnetic bead positioned at the catheter or guidewire tip[22], are capable of producing higher forces than their Lorentz torque-based counterparts. Nonetheless, they introduce greater signal noise into MR images[14,22] due to interference with the imaging sequences, and, unlike solenoid coil systems, their magnetization cannot be deactivated to achieve artifact-free imaging.

To tackle the challenges of controlled actuation and navigation within the MRI environment, we introduce a novel MRI-driven robotic guidewire system. Building upon prior work in the field[14,16,28,29], our approach features a magnetic tip connected by a soft medical suture to a wire housed within an insertion device, functioning as a guidewire (illustrated in Figure 1). By leveraging the magnetic field gradients inherent to MRI systems, we achieve selective actuation of the magnetic tip in arbitrary directions, enabling navigation through complex pathways. The magnetic tip is incrementally advanced (approximately 10 mm) using gradient forces, after which a sleeve is advanced along the tether to follow the trajectory established by the tip. This technique ensures that the guidewire faithfully tracks the motion path of the tip, allowing for precise control of position and direction.

Importantly, we demonstrate for the first time the tangential actuation—aligned with the direction of motion—of a tethered system using MRI gradient forces. By combining this tangential motion with perpendicular steering capabilities, our method enables effective MRI-driven manipulation of a tethered milli-robot, specifically designed for endovascular interventions. Furthermore, we investigate how the presence of the robot affects MR image quality, providing experimental insight that lays the groundwork for future development of a closed-loop control system based on this platform.

[R1.2] Lalande et al[22] proposed a similar design, featuring a guidewire with a chrome-steel bead attached at the tip. Their approach enabled advancement of the guidewire through the anatomy via mechanical push force, while steering was achieved through MRI gradient actuation of the magnetic bead. However, there are several key distinctions between their work and the approach presented in this paper. Notably, their system utilized a rigid tool that required mechanical pushing for advancement, whereas our design employs a soft, flexible tool that is actuated purely through magnetic gradient pulling. The rigidity of their system inherently limits navigational capabilities, particularly making retroflection difficult, while our soft tool can negotiate sharper anatomical curves, and minimizes the risk of tissue damage. The gradient pulling mechanism is fundamental in enabling the softness of the device, which constitutes a central innovation of our work. Another difference compared to the design in Lalande et al[22] is the exploration of multiple materials, systematically analyzing their magnetic responses, and characterizing the associated MR signal noise.

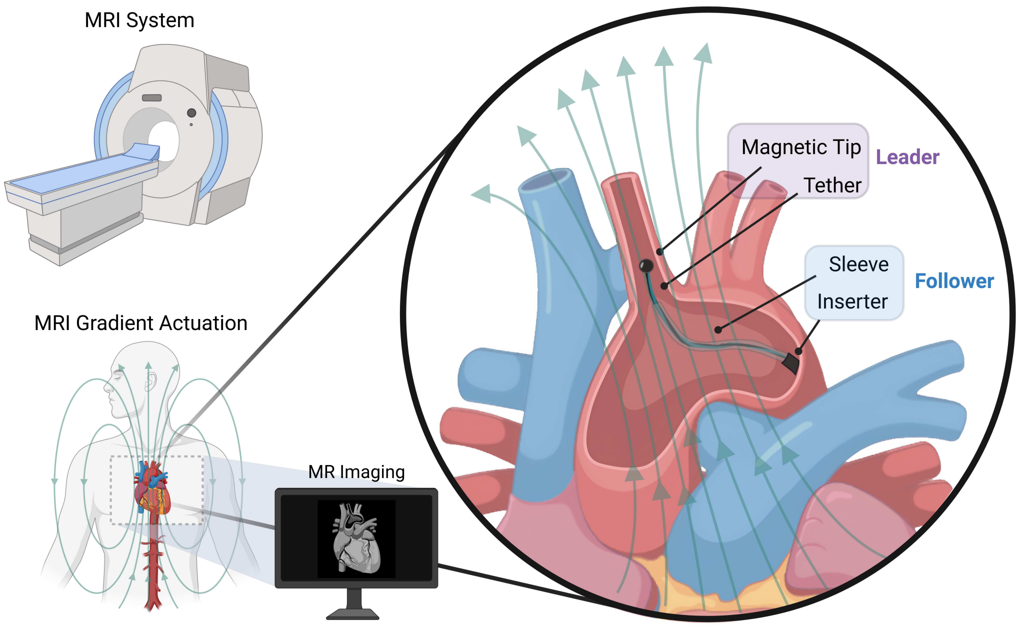

Figure 1. Visualization of an MRI-controlled robot functioning as a guidewire for cardiovascular navigation within an MRI system.

The magnetic tip is actuated using the MRI system's magnetic gradients to guide navigation toward the targeted pathology. The tether follows the tip, subsequently, the sleeve can reach the area of interest by following the tether.
Created in BioRender. Murasovs, N. (2025) https://BioRender.com/c45f936

RESULTS

The leader-follower approach we adopt combines a low material stiffness at the most distal end of the robot (the leader) to minimize potentially harmful mechanical push forces and a flexible sleeve (follower) that advances along the pathway of the leader. In this design (depicted in the popout in Figure 1), a magnetic tip of the leader (we use a steel sphere tethered to a thin silk wire) is guided incrementally along a predefined pathway via gradient actuation of the MRI system. An overlapping sleeve follows the trajectory established by the tip to stabilize the shape of the robot. This process is repeated until the target location is attained. This system establishes a guidewire, allowing for the subsequent addition of more conventional tools through or around the sleeve.

The navigation process thus follows an incremental three-step sequence: (a) The tether is released some small distance ($\sim$10 mm) to provide freedom for the tip to move in any direction. (b) The magnetic tip of the leader is pulled by forces generated by magnetic field gradients in 3D. (c) The overlapping flexible sleeve (the passive follower) subsequently advances along the trajectory established by the leader, aligning its tip with the magnetic tip's position to stabilize the system. This process is then repeated as the next navigation step.

Imaging and actuation cannot be performed simultaneously but can be interleaved at frequencies greater than 1 Hz. In this study, an MR Imaging sequence is performed after each third step to confirm successful step-wise navigation.

Principles of MRI Actuation

MRI utilizes strong magnetic fields and radiofrequency pulses to generate detailed images of internal tissues. The MRI system consists primarily of a static magnetic field, $\vec{B}_0$, clinically typically in the range of 1.5T to 3T (our system, a preclinical Bruker BioSpec 70/20 MRI system, produces a background field of 7T), and a set of tri-axial magnetic field gradients, in our case with a maximum magnitude of 660 mT/m, used during imaging to obtain spatial information on the sample. The $\vec{B}_0$ field provides a uniform magnetic environment that aligns the nuclear spins of hydrogen protons within the body, forming the foundation for image generation. These features are essential for imaging but also form the basis for magnetic actuation in robotic applications. Applying a magnetic gradient field $\nabla\vec{B}$ (which superposes the main magnetic field but varies linearly in three orthogonal axes) generates a magnetic force on any ferromagnetic body inside the MRI system:

$$\vec{F}_m = V\left(\vec{M}\cdot\nabla\right)\vec{B} \tag{1}$$

where V is the volume of the ferromagnetic body and ($\vec{M}$) is the magnetization vector of the ferromagnetic body, (∇) is the vector differential operator, and ($\vec{B}$) is the magnetic field vector[30].

MRI-compatible actuation in soft robots operates by balancing the internal elastic energy of the robot with the influence of an externally applied magnetic field gradient. To date, traditional magnetic robotic systems have relied on hard magnetic remanence stored within the robot's material, combined with a relatively low externally applied magnetic field[10]. The interaction between these internal and external fields generates a magnetic torque, which is then translated into deformation for shape forming[31] or propulsion[32].

However, within the bore of a high-field MRI system, the static background field ($\vec{B}_0$) is sufficiently strong that any magnetic remanence in the robot's material is effectively erased. As a result, robots with remanent magnetization profiles are unable to maintain their intended magnetization patterns[15,33,34] and this renders the concept of "hard magnetization" redundant, making the well-established approaches to magnetic actuation incompatible with MRI environments.

Consequently, new methods must be devised to leverage the strong, uniform $\vec{B}_0$ field and dynamic magnetic gradients ($\nabla\vec{B}$) for precise actuation, while adhering to the unique constraints of the MRI setting.

Furthermore, soft-magnetic objects that are not uniformly symmetrical, for instance, shapes with a unique axis of symmetry, will experience the preferential direction of magnetization known as "easy axis"[35]. This phenomenon will result in a permanent alignment of this axis with the magnetic field ($\vec{B}_0$) of the MRI system which would fixate the object's orientation, disallowing any gradient-induced changes. Therefore, following these studied phenomena, we can establish soft magnetics as a material choice for our robot, and a spherical design as the necessary choice of shape[14,16,28,29].

Due to the magnetic saturation of ferrous objects under the static magnetic field, $\vec{B}_0$, which is aligned along the z-axis in MRI systems, the magnetization direction of ferrous objects becomes aligned with $\vec{B}_0$. Consequently, the magnetization vector for any ferrous object in an MRI system can be expressed as:

$$\vec{M} = \begin{bmatrix} 0 & 0 & M_s \end{bmatrix}, \tag{2}$$

where M_s represents the saturation magnetization of the ferrous object inside the MRI.

By substituting Equation (2) into Equation (1) and applying the gradient operator $\nabla = \begin{bmatrix} \frac{\partial}{\partial x} & \frac{\partial}{\partial y} & \frac{\partial}{\partial z} \end{bmatrix}^\top$, we derive:

$$\vec{F}_{\text{gp}} = V M_s \begin{bmatrix} \frac{\partial B_z}{\partial x} \\ \frac{\partial B_z}{\partial y} \\ \frac{\partial B_z}{\partial z} \end{bmatrix}. \tag{3}$$

As $\vec{B}$ is dominated by field in the Z direction, magnetic gradients generated by the MRI gradient coils are defined as $\vec{G}_{\text{MRI}} = \begin{bmatrix} \frac{\partial B_z}{\partial x} & \frac{\partial B_z}{\partial y} & \frac{\partial B_z}{\partial z} \end{bmatrix}^T$. Using this definition, the magnetic gradient pulling force can be expressed as:

$$\vec{F}_{\text{gp}} = V M_s \vec{G}_{\text{MRI}} \tag{4}$$

Equation (4) highlights the ability of an MRI system to generate a magnetic pulling force within the three-dimensional space $\mathbb{R}^3$.

Image Distortion

The introduction of any ferromagnetic object into an MRI scanner results in image distortions due to the interference of the object's magnetic field with the main magnetic field[6,16,29]. This causes artifacts that degrade image quality and spatial resolution. The extent of this distortion is influenced by the choice of material, shape, and volume of the object[36] but also by the type of imaging sequence/choice of acquisition parameters. Therefore, there is a trade-off: on one hand, larger magnetic materials with higher saturation are desirable for generating greater forces, allowing stronger actuation under the MRI's gradient fields; on the other hand, these same properties can lead to significant larger artifacts/signal voids on MR images, compromising image quality and diagnostic utility. Figure 2 illustrates a comparison of the image distortions produced during an MR sequence by chrome steel (AISI 52100[37]) balls and low-carbon steel (AISI 1010[38]) balls of 1 mm and 1.5 mm diameters. Figure 2 highlights the differences in signal voids generated by the two materials across both sizes.

To quantify the signal voids produced by each ball in Figure 2, we use the pixel spacing of 0.078125 mm $\times$ 0.078125 mm, which is given by the image size ('field-of-view') divided by the number of points in each dimension. This spacing indicates that each pixel has an area of approximately 0.006104 mm^2. Therefore, the signal voids can be determined by counting the number of pixels below a set threshold (here: gray scale value below 50 was used, out of max value of 255) in the generated images and multiplying this count by the corresponding scaling factor. The findings of this analysis are summarized in Table 1, along with the corresponding ratio of void area to object's maximal cross-sectional area.

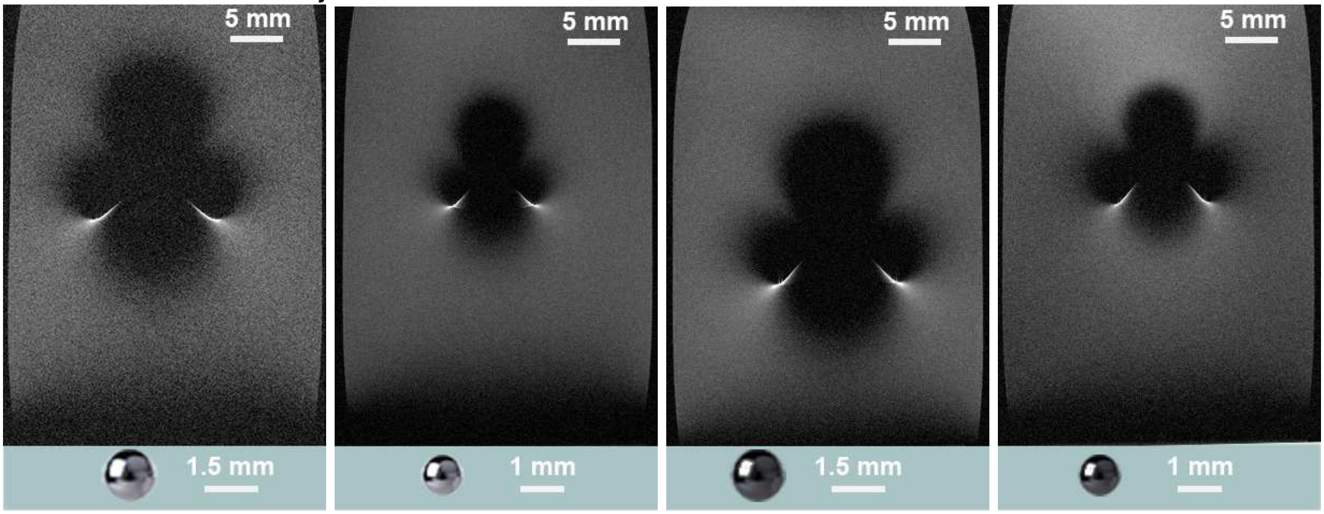

Figure 2. Examples of signal noise in magnetic resonance imaging caused by the presence of ferromagnetic objects.

Shown are: (A) a chrome-steel ball (AISI 52100[37]) with a diameter of 1.5 mm, (B) a chrome-steel (AISI 52100[37]) ball with a diameter of 1.0 mm, (C) low-carbon steel (AISI 1010[38]) ball with a diameter of 1.5 mm, and (D) low-carbon steel (AISI 1010[38]) ball with a diameter of 1.0 mm. The MR images were generated by embedding the balls in 1% agarose solution, doped with 5 nM Gadolinium (Dotarem) and imaged on a preclinical Bruker BioSpec 7T MRI system using a multi-slice, spin echo sequence (TTE/TR = 2.7/1,000 ms, matrix size of 512x512, field-of-view of 40x40 mm, slice thickness of 0.5 mm, bandwidth of 500 kHz).

Table 1. Summary of the noise area detected in MR images

	Diameter, D_s (mm)	Noise (mm^2)	Ratio
Chrome Steel	1.5	247	140
	1.0	137	175
Low-carbon Steel	1.5	293	166
	1.0	142	181

Summary of the noise area detected in MR images for chrome steel and low-carbon steel balls with diameters of 1.5 mm and 1.0 mm, along with the corresponding ratio of noise area to the object's maximal cross-sectional area.

Magnetic Characterization

Pure iron or iron-cobalt alloy (such as Fe-49Co-2V) are documented to have the highest magnetic saturations[39], which would result in a stronger response to the MRI's gradient fields; however, they are impractical as they corrode when exposed to moisture, making them unsuitable (in their uncoated form) for medical applications. Furthermore, manufacturing pure iron spheres is challenging, as all production methods known to the authors introduce carbon impurities, compromising the material's magnetic properties.

The magnetic force response of an object in a magnetic gradient depends on its magnetic saturation and volume[30]. We evaluated the magnetic response of both chrome steel (as used in[14] and[23]) and our low-carbon steel samples. Their magnetization hysteresis curves were measured using a superconducting quantum interference device - vibrating sample magnetometer (SQUID-VSM) - MPNS3 from Quantum Design, UK. The experiments were conducted at a temperature of $36.7°C$ and under atmospheric pressure to simulate clinical operating conditions.

The magnetic saturation of chrome steel occurs at approximately 0.70 emu (1.69 T) (see Figure 3), while the magnetic saturation of low-carbon steel is measured at 0.98 ± 0.02 emu (2.37 ± 0.05 T). With Equation (4) this indicates the magnetic force response of low-carbon steel balls to the MRI gradient is approximately 40% greater than that of chrome steel balls of the same size. The enhanced response of low-carbon steel is likely attributable to the absence of chromium and, therefore higher iron content (a more detailed analysis of the physics of this behavior, whilst undoubtedly interesting, is out of scope for this work). It is relevant to highlight that the low carbon steel balls corrode/oxidize significantly faster than the chrome steel balls - a matter of days as opposed to weeks - which is inconsequential for a disposable guidewire design but inconvenient for experiments conducted over multiple days.

The variation in magnetization curves between the two low-carbon steel samples is likely attributed to the low precision in the size and shape of the balls. Further details are provided in Table 2. In contrast, chrome steel balls exhibit minimal diameter error as they are commercially produced for use as mechanical ball bearings, where high sphericity is a strict requirement. Conversely, the low-carbon steel balls were likely manufactured for less exacting use cases, leading to higher errors in their sphericity and measured diameter.

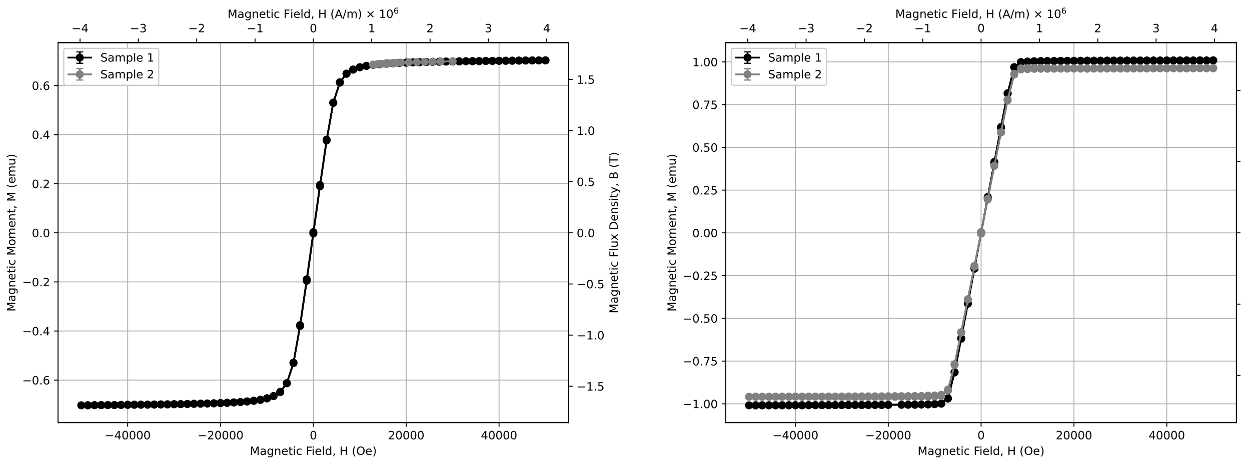

Figure 3. Magnetization curves of ferromagnetic objects.

Shown are: (A) 1 mm chromium steel, (B) 1 mm low-carbon steel, obtained using a commercial SQUID-VSM (superconducting quantum interference device - vibrating sample magnetometer) machine (MPMS3, Quantum Design, UK). The curves for the two repeat samples are shown in black and gray, respectively. Error bars are included but are not visible due to the minimal error at each data point. The plot shows the relationship between the magnetic field (in units of Oe and A/m) and magnetization (in units of emu). Induced magnetic flux density (in units of B) is provided on the right y-axis for reference.

Table 2. Comparison of the manufacturer-specified ball diameters with the measured diameters.

		Measured values (mm)	
	Diameter, D_s (mm)	Diameter, D_m	S.D.
Chromium Steel	1.5	1.4937	0.0048
	1.0	0.9930	0.0047
Low-Carbon Steel	1.5	1.4891	0.0079
	1.0	0.9975	0.0243

Comparison of the manufacturer-specified ball diameters, D_s, with the measured diameters obtained for chrome and low-carbon steel. The measured diameters, D_m, were determined across 20 samples using a micrometer-scale electronic caliper. The standard deviation errors associated with the measurements are listed in the final column.

Magnetic Pulling Force

Using the magnetic response results from section above, we can compute the potential range of forces that an MRI system can generate to navigate the robotic guidewire. To convert the magnetic saturation values (M_s) from magnetic flux density (T) to magnetization (A/m), we use the following equation[30]:

$$M_s = B_s/\mu_0 \tag{5}$$

where $\mu_0 = 4\pi \times 10^{-7}\ T \cdot m \cdot A^{-1}$ represents the permeability of free space, and the values for B_s are provided in the section above.

As mentioned before, the maximum magnetic gradient strength produced by the MRI system in our experimental setup is 660 mT/m. Consequently, throughout the remainder of the paper, a gradient strength of 30% corresponds to approximately 198 mT/m, while 90% (the maximum gradient achievable within the constraints of the duty cycle) corresponds to around 594 mT/m. Table 3 summarizes the magnetic gradient amplitudes utilized throughout this manuscript. By inserting these values into Equation 4, the gradient pulling force is determined. The corresponding values are summarized in Table 4. In our system, a 1 mm diameter chrome steel ball experiences a maximum pulling force of 0.41 mN at 90% gradient strength, while a low-carbon steel ball of the same size reaches 0.58 mN under the same conditions. As a result, substituting chrome steel balls with low-carbon steel balls increases the pulling force by roughly 40%.

Table 3. Magnetic gradients of the MRI system

	at 30%	at 50%	at 70%	at 90%
Magnetic Gradient (mT/m)	198	330	462	594

Magnetic gradients of the MRI system at various strengths relative to the maximum gradient strength specified by the manufacturer.

Table 4. Summary of the variables, values, and units used in the calculation of the magnetic pulling force

Material	Variable	Units	Value	S.D.
Chromium Steel	V	m^3	5.13×10^{-10}	7.28×10^{-12}
	B_s	T	1.69	-
	M_s	A/m	1.35×10^6	-
	$F_{\text{gp,30}}$	N	1.37×10^{-4}	1.94×10^{-6}
	$F_{\text{gp,90}}$	N	4.10×10^{-4}	5.82×10^{-6}
Low-Carbon Steel	V	m^3	5.20×10^{-10}	3.80×10^{-11}
	B_s	T	2.37	0.05
	M_s	A/m	1.89×10^6	3.98×10^4
	$F_{\text{gp,30}}$	N	1.94×10^{-4}	1.48×10^{-5}
	$F_{\text{gp,90}}$	N	5.82×10^{-4}	4.43×10^{-5}

Summary of the variables, values, and units used in the calculation of the magnetic pulling force for 1 mm diameter balls. Here, V represents the volume of the ferrous object, B_s and M_s denote the magnetic saturation in terms of magnetic flux density and magnetization, respectively, and F_{gp} is the gradient pulling force, shown for 30% and 90% gradient strengths.

Leader-Follower Friction

The effectiveness of the proposed robotic guidewire design relies significantly on the system's ability to incrementally pull the magnetic tip to a target location, followed by extending the sleeve along the defined pathway. In this navigation approach, the material properties of the sleeve dictate the intrinsic friction forces encountered during the process. These forces affect both the pulling of the magnetic tip and thread from the sleeve, as well as the subsequent sliding of the sleeve along the pre-defined trajectory to reach the intended position.

To investigate this, we designed an experiment based on the study conducted by[40], where the authors employed tribology research equipment to analyze friction forces generated by the sliding of Vicryl medical suture against porcine tissues. In our case, we developed an experimental setup to evaluate the friction forces by pulling the Vicryl suture through a 30 mm segment of our silicone sleeve. The measurements were recorded using a Modular Tribometer (Bruker UMT TriboLab, US) machine. An overview of the experimental setup is provided in Figure 4(a).

The data were analyzed using a Fourier transform to identify resonant frequencies of acoustic oscillation within the frequency range of data acquisition. Once any significant acoustic resonant peaks were identified, a series of simple-moving-average (SMA) filters were applied in descending order of each identified resonant frequency to remove their influence and isolate a time-averaged trace for frictional resistance. Low-frequency broad-band acoustic oscillations were mostly observed centered around 320 Hz, 200 Hz, 150 Hz, and 125 Hz respectively, with each peak exhibiting a bandwidth full width at half maximum (FWHM) of around 10 Hz. These oscillations originate from localized stick-slip friction regime transitions along the length of the thread-sleeve contact (see Figure 4(b)). From Figure 4(b), we can infer that a force of approximately 0.5 mN is needed to overcome the system's friction in this arrangement. This corresponds to a 77.42% gradient strength, equivalent to 511 mT/m, for the 1 mm low-carbon steel ball.

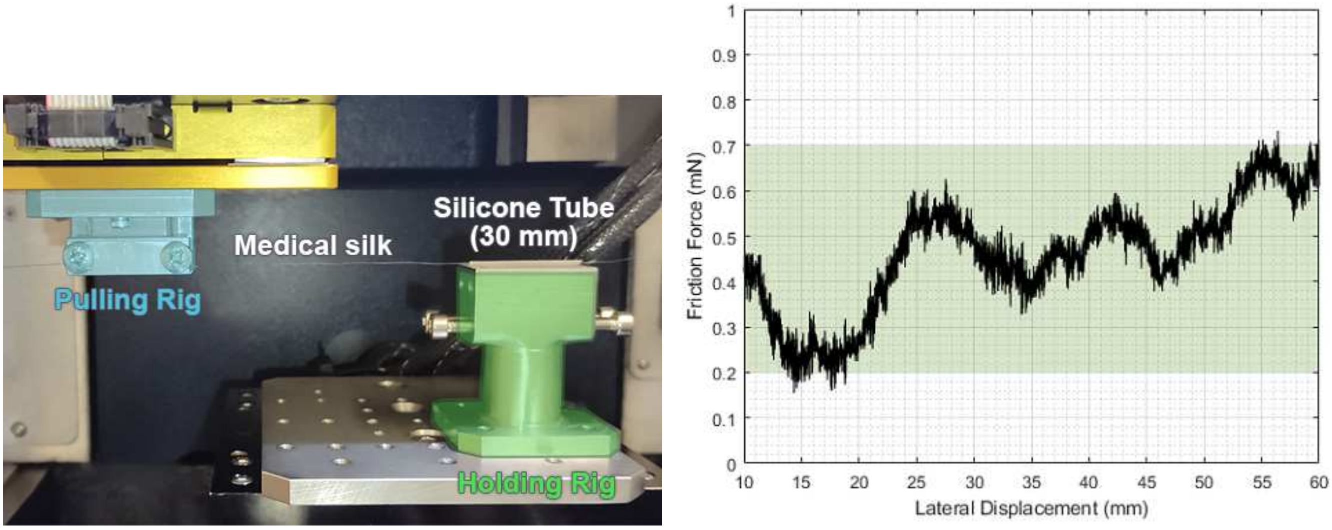

Figure 4. Summary of the tribology analysis performed for the robotic guidewire.

(A) Photograph of the experimental setup, highlighting the pulling rig, holding rig, and labeled components, including the silicone sleeve and medical suture. (B) Time-averaged friction force (after applying simple moving averages at 320 Hz, 200 Hz, 150 Hz, and 125 Hz, sequentially) across lateral displacement from the thread being drawn through the sleeve. The green area denotes the span of observed friction forces.

Robot Design & Principles of Navigation

A critical consideration in the design of MRI-actuated robotic systems is balancing the trade-off between actuation response and MR image distortion. Effective actuation ensures reliable robot movement while minimizing artifacts is essential for maintaining image clarity.

The tether serves as a connection between the robot's tip and its base, enabling controlled movement. Additionally, a mechanism must be implemented to allow the tether to reliably follow the tip trajectory to the target location. The tether material must be lightweight, exhibit low friction, and be biocompatible. Medical VICRYL (polyglactin 910) suture thread was selected according to these properties.

For the follower sleeve, we selected a silicone tube with an inner diameter of 0.51 mm and an outer diameter of 0.94 mm from HelixMark (Ref Number: 60-411-41). This choice was driven by the sleeve's low stiffness (Tensile strength of 9.55 MPa, Shore Hardness of 55 A, approximate Young modulus of 47 MPa[41]) which facilitates greater bending flexibility, and its low surface friction (by silicone standards - see section above), which minimizes drag forces between the tether and the sleeving tube, ensuring smooth sliding.

The choice of magnetic tip was guided by balancing the considerations of image distortion, pulling strength, and size. Based on consideration of these factors from the previous sections we selected a 1 mm low-carbon steel ball bearing which best meets the imaging and actuation requirements of the options we explored.

The magnetic pulling forces exerted on a 1 mm low-carbon steel ball by MRI gradients (as listed in Table 4) align closely with the friction forces measured at 30 mm along the silicone sleeve, as shown in Figure 4. This demonstrates a strong compatibility between the proposed follower design and the selected magnetic tip material and shape, based on the generated pulling forces. The friction forces within the system are directly influenced by the length of the sleeve. If the sleeve is too long, the pulling force may become insufficient to overcome the friction force, thereby imposing an upper limit on the sleeve length that can be effectively used in this design. In this study, a 30 mm silicone sleeve was used for most experiments, except for the maze phantom navigation (refer to the section below), where a 50 mm silicone sleeve was utilized.

Experimental Setup

For the actuation and imaging during the experiments, a pre-clinical MRI system, a Bruker BioSpec 70/20, equipped with a 660 mT/m gradient system (inner diameter (id) 120mm) and a quadrature-driven birdcage radio frequency (RF) coil (id: 72mm), was utilized. To document the experimental procedures and validate the resulting MR images, two 3.9 mm diameter 720P MRI compatible endoscopic cameras (Shenzhen Licam Technology Co., Ltd.) were positioned on opposite sides of the workspace, as illustrated in Figure 5(b). These cameras provided detailed visual coverage to complement the MRI-based observations. Additional details regarding the experimental setup can be found in Figure 5.

To actuate the magnetic tip of the leader, we applied MRI gradients of varying strengths, ranging from 30% to 90% (with specific values detailed throughout the paper), along with a pulse duration of 100 ms and a repetition time of 500 ms. At the maximum gradient strength of 90%, this corresponded to approximately 42% of the MRI system's duty cycle, which was identified as the system's operational limit. This actuation sequence enabled the magnetic tip to be pulled for 100 ms, followed by a 400 ms interval before the next cycle. During each actuation step, the magnetic tip was set in motion, and the repeated application of the actuation signal facilitated quasi-continuous navigation.

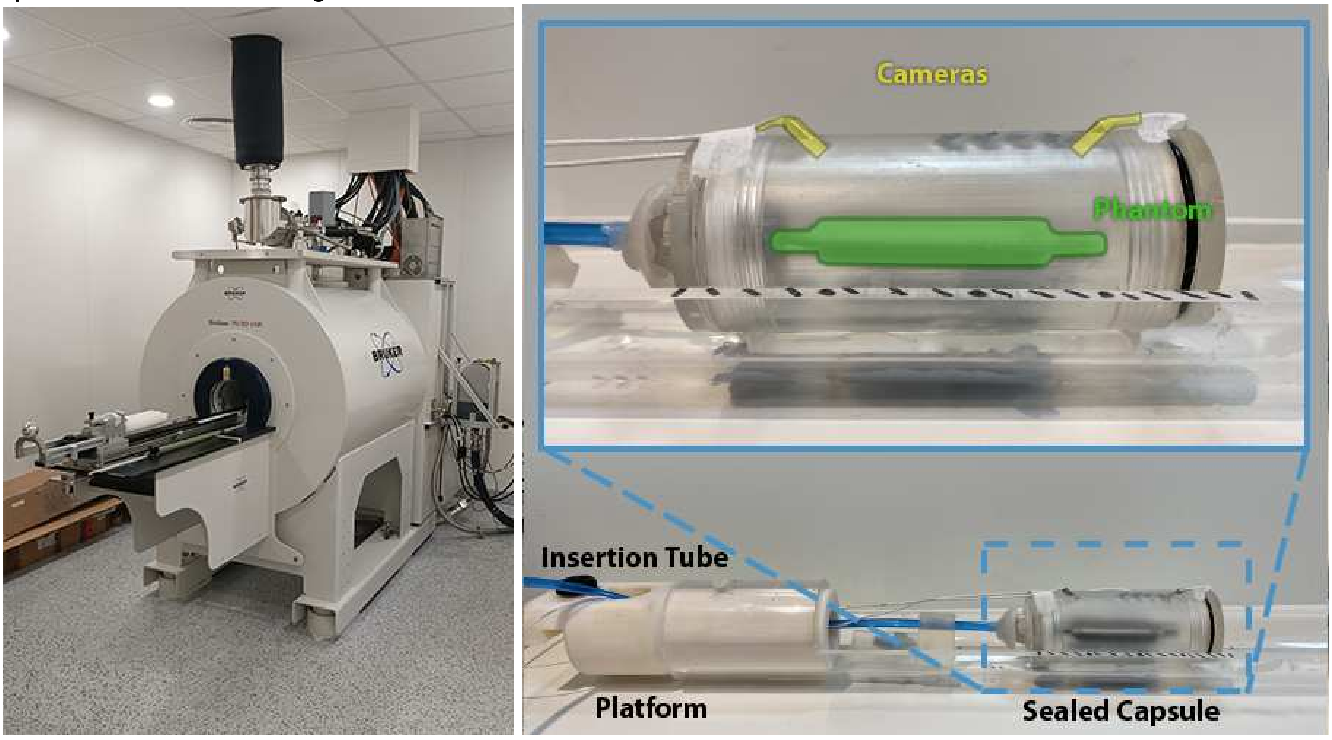

Figure 5. Overview of the experimental setup.

(A) Bruker 7T pre-clinical MRI system, and (B) the platform inserted into the MRI system, showing the insertion tube and sealed capsule; a close-up view of the sealed capsule highlights the phantom (in green) and endoscopic cameras (in yellow).

Manufacturing

The manufacturing process for the robotic guidewire, is presented in Figure 6 and involves the following steps:

1. A ferromagnetic ball is secured on a microscope glass slide with a sticky surface to prevent the ball from moving.
2. The glass slide is viewed under a microscope, and medical silk is attached to the steel ball using water-resistant EverBuild Stick2 Industrial Grade HV superglue.
3. The free end of the medical silk (total length of 50 mm, where 30 mm for the silicone sleeve and 20 mm for the unconstrained tether) is attached to a thin nitinol guidewire (McMaster of 0.01 inches outer diameter) with industrial superglue, cured, and then threaded through a thin silicone sleeve (30 mm) with an outer diameter of 0.94 mm.
4. Once the silk is threaded through the silicone sleeve, the nitinol guidewire is cut and removed.
5. The new cut/free end of the silk is glued to a larger nitinol rod (McMaster 0.03 inch of outer diameter), which will act as the mechanism for adjusting the insertion length during operation.
6. The nitinol rod and its subsequent connection are threaded into a PTFE tube. The ends of the PTFE tube and the silicone sleeve are secured together using industrial superglue.

After every application of industrial superglue, the arrangement is cured in standard atmospheric conditions for 30 minutes at room temperature. Industrial-grade HV superglue from EverBuild was utilized for securing components. See Figure 6 for the overview of the manufacturing process for the robotic guidewire. All materials, except for the low-carbon steel ball, are biocompatible, as low-carbon steel is prone to corrosion in water.

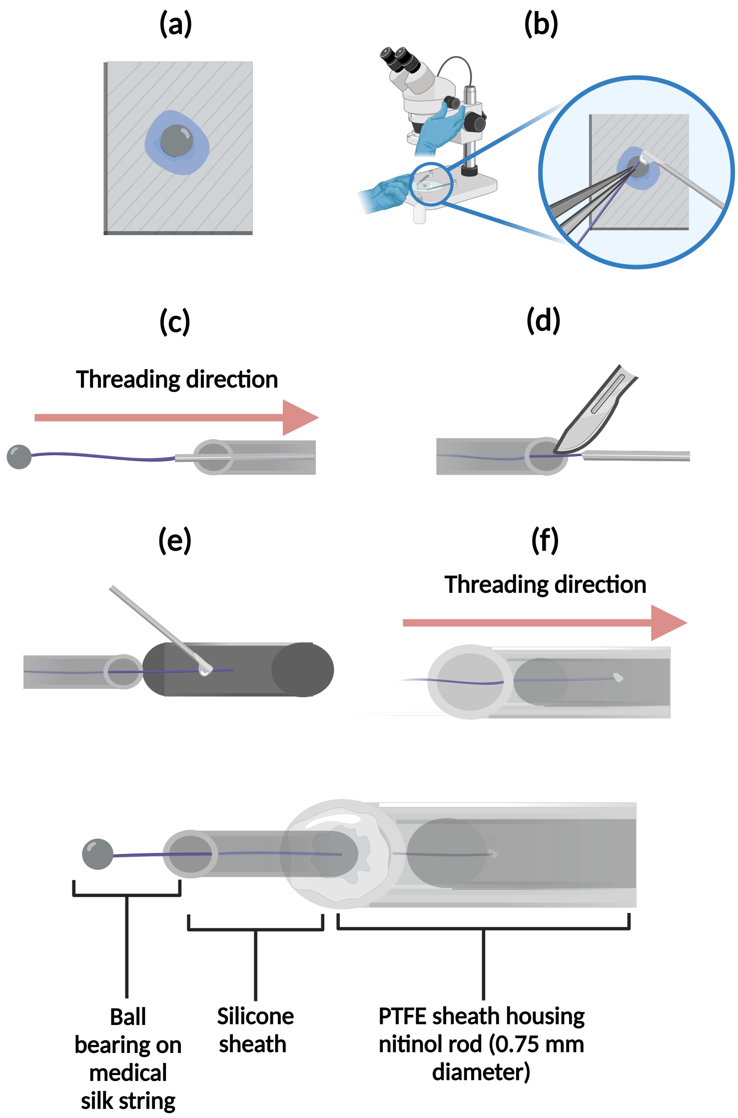

Figure 6. Outline of the manufacturing process for the tethered robotic guidewire, detailing the sequential steps involved in assembling the components.

Shown are: (A) the ball secured on a microscope glass slide, (B) the attachment of the ferromagnetic ball bearing, (C) threading of the medical silk through the silicone sleeve, (D) cutting the thin nitinol guidewire once the silk is threaded, (E) integration with the nitinol rod, and (F) threading the nitinol rod through the PTFE tube to allow human operation from outside the MRI system.
Created in BioRender. Bacchetti, A. (2025) https://BioRender.com/s54f473

Deformation Characterization

The robotic guidewire's physical response to MRI gradients is a critical aspect of this navigation method. The magnetic tip achieves magnetic saturation at all times in the MRI bore due to the high background field. The maximum applicable force thus corresponds to the range of magnetic gradients that the MRI system can generate. Achievable deformations and tangential motion are then a function of the robot's design.

To optimize the device's performance and provide the operator with an intuitive understanding of how various gradient strengths influence the magnetic tip and deform the guidewire, we conducted a deformation characterization study. This study evaluates the system's response to different MRI gradient strengths. The robotic guidewire was tested in multiple configurations, varying the length of the tether extending from the sleeve (unconstrained tether) and the length of the sleeve itself. The system was actuated under gradient strengths of 30%, 50%, 70%, and 90% in the X-direction (see Figure 7(b) for the reference of the basis frame). Both positive and negative gradient strengths were applied to counteract the effects of any manufacturing-induced prebend in the sleeve, with the results representing the average response between positive and negative tests (see Figure 8).

To achieve these results, the robotic guidewire was secured within a rigid tube of matching diameter to minimize undesired horizontal motion of the system's base. This setup allowed manipulation of the lengths of the tether and sleeve, enabling various configurations with differing amounts of tether and sleeving. In total, we evaluated eight different configurations, which can be divided into two groups: (1) setups without an unconstrained tether, consisting of sleeve lengths of 5 mm, 10 mm, 15 mm, and 20 mm; and (2) setups with a constrained tether while maintaining a total length of 20 mm, including combinations of a 15 mm sleeve with a 5 mm tether, a 10 mm sleeve with a 10 mm tether, a 5 mm sleeve with a 15 mm tether, and a configuration with no sleeve (0 mm) and a 20 mm tether. A summary of the achievable range of motion for the system is presented in Figure 8.

The experiment was captured using the cameras described in the section on experimental setup, with an example frame of the scene shown in Figure 7(a) for reference. A green background was utilized to enhance the segmentation process, while a checkerboard strip at the top of the frame was employed to transform the scene into the horizontal plane. The captured frame was corrected for physical lens distortions through a camera calibration process using OpenCV Camera Calibration code in Python[42], and the checkerboard pattern was used to apply a homography transformation, ensuring the result was represented in a purely horizontal domain to enable the characterization process (see Figures 7(a-b) and note the placement of the purple lines). Once the frame was transformed into the horizontal domain, the robot was segmented by applying Gaussian blur, adaptive binary thresholding (in the HSV color space), and a sequence of erosion and dilation operations, leaving only the robot with the background removed. Subsequently, curve fitting was performed to digitally reconstruct the robotic guidewire's shape, leveraging the known real-world lengths of the tether and follower's sleeve (see Figure 7(c)). The blurriness observed at the tip of the robot indicates uncertainty in its position during operation, which was used to derive the error margins shown in Figure 8. Finally, using the reconstructed shape of the robot in the digital domain, we plotted the range of motion across various MRI gradient strengths and different robotic guidewire configurations. A summary of these findings is presented in Figure 8.

To explore the relationship between the range of motion of the robotic guidewire and the applied MRI gradient strength, we define three key metrics:

1. Final Tip Inclination (*FTI*): This metric evaluates the position of the sleeve's tip at the deformed state of the actuation sequence. It provides insights into the robotic guidewire's ability to achieve sharp angles during navigation, as the deformed position of the body is a critical factor in directional control. It is measured as the angle between the sleeve tip and the vertical axis.

2. Deformation Range (*DR*): This metric quantifies the robot's range of motion by measuring the horizontal displacement of the sleeve's tip between its responses to -90% and 90% gradient strengths.

3. Min-to-Max Deformation Ratio (*MMDR*): This metric represents the ratio of the area covered in the range of motion at 30% gradient strength to that at 90% gradient strength. It

highlights the difference between configurations that allow a broad, fully controllable range of motion and those where the robotic guidewire becomes highly deformed, reducing stability and controllability between referential and deformed states.

A depiction of these metrics is presented in Figure 7(d), while Figure 9 provides a comparison between configurations with and without unconstrained tether across various sleeve lengths. Refer to Supplementary Video 1 for the demonstration.

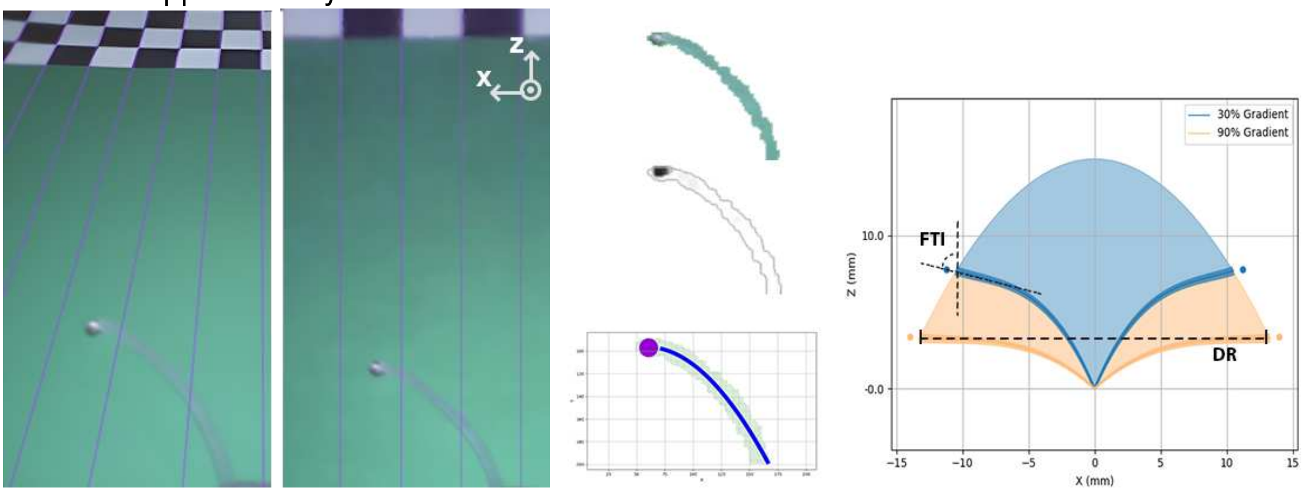

Figure 7. Overview of the segmentation process used to analyze deformations of the robotic catheter.

(A) Real-world image of the experiment conducted for deformation characterization, displaying the raw video stream, with a checkerboard pattern at the top of the screen serving as a reference for plane reconstruction. (B) Processed output frame after applying camera calibration and homography transformation, with purple lines indicating the transformation of the underlying plane. (C) Visual representation of the robotic guidewire (top), intermediate results from the image processing steps Gaussian blur, dilation, erosion, and binary thresholding (middle), and the final curve-fitting output for the digital reconstruction of the robot (bottom). (D) Results of the deformation characterization analysis, illustrating the full range of motion, with blue representing 30% gradient strength and orange representing 90% gradient strength. These regions are utilized to calculate the MMDR metric. The image also includes schematics for the Deformation Range (DR) and Final Tip Inclination (FTI) metrics.

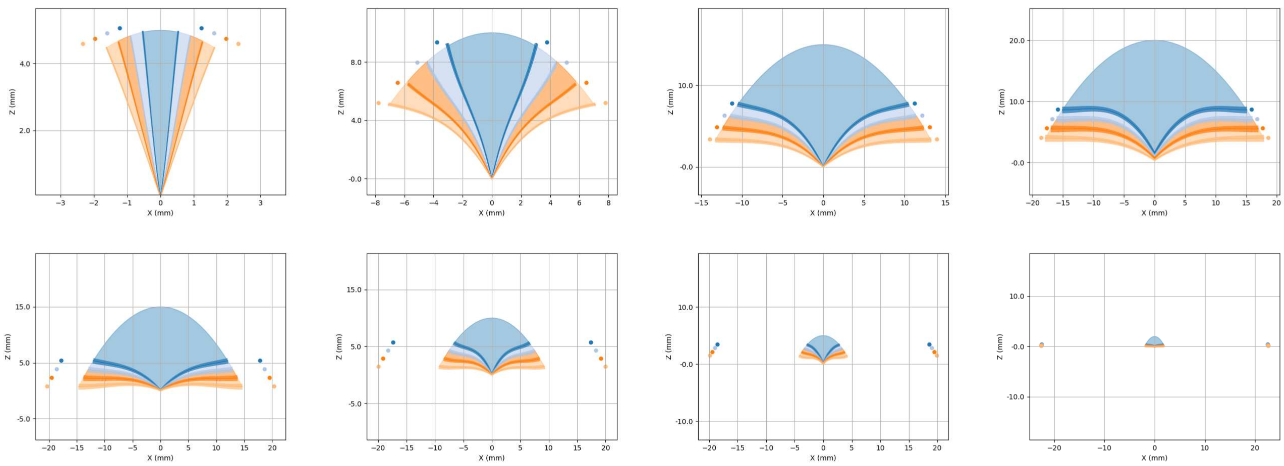

Figure 8. Summary of the deformation characterization range of motion, showcasing the robotic guidewire configured with varying lengths of sleeving and unconstrained tether.

Deformation testing was conducted at four distinct gradient strengths in the X-direction: 30% (blue), 50% (light blue), 70% (orange), and 90% (light orange), using both positive and negative gradient strengths. This approach eliminates the influence of manufacturing-induced prebent deformation of the sleeve. The resulting curves represent the average response between the positive and negative gradient tests. The reference positions of the magnetic tip at the end of the tether are also indicated. The varying thickness of the curves illustrates the positional uncertainty of the robot during frame capture. Where: (A) 5 mm sleeve, 0 mm unconstrained tether, (B) 10 mm sleeve, 0 mm unconstrained tether, (C) 15 mm sleeve, 0 mm unconstrained tether, (D) 20 mm sleeve, 0 mm unconstrained tether, (E) 15 mm sleeve, 5 mm unconstrained tether, (F) 10 mm sleeve, 10 mm unconstrained tether, (G) 5 mm sleeve, 15 mm unconstrained tether, and (H) 0 mm sleeve, 20 mm unconstrained tether.

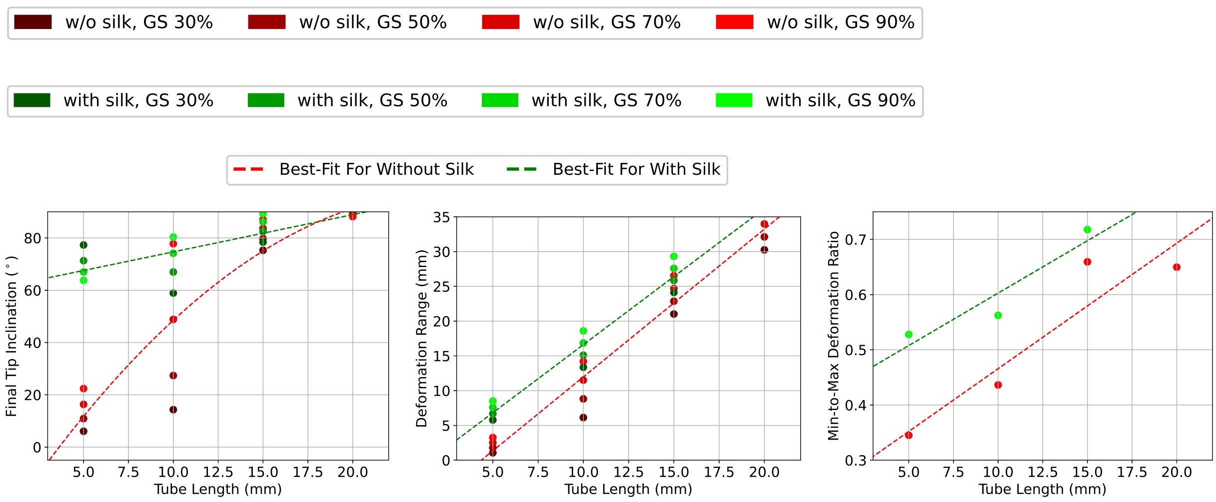

Figure 9. Overview of deformation characterization metrics relative to sleeve lengths, comparing configurations with medical silk (unconstrained tether) to those without.

This plot highlights the impact of the unconstrained tether on the final position of the sleeve, the robotic guidewire's range of motion, and the controllability of that range. Configurations with the unconstrained tether are represented in green, while those without (where the magnetic tip is positioned at the tip of the sleeve) are shown in red. For (A) and (B), different shades of green and red indicate gradient strengths, with the brightest shades representing 90% gradient strength and the darkest shades representing 30% gradient strength. Where: (A) Final Tip Inclination, (B) Deformation Range, and (C) Min-to-Max Deformation Ratio.

Gradient Pulling Analysis

The ability of the magnetic tip (steel ball) to be pulled by the gradient is highly influenced by the curvature of the silicone sleeve. To evaluate this dependency, an experiment was designed to demonstrate the feasibility of tangential gradient pulling of the tethered soft robot through a pre-deformed tube. For this purpose, a phantom was constructed with predefined curvature radii (see Figure 10(b) for reference), enabling the assessment of the minimum gradient strength required to pull the magnetic tip. The experiment was conducted using three different phantoms with curvature radii of 15 mm, 20 mm, and 25 mm, with each condition repeated three times to ensure reproducibility. Additional details on the setup are illustrated in Figure 10, while the results are summarized in Table 5.

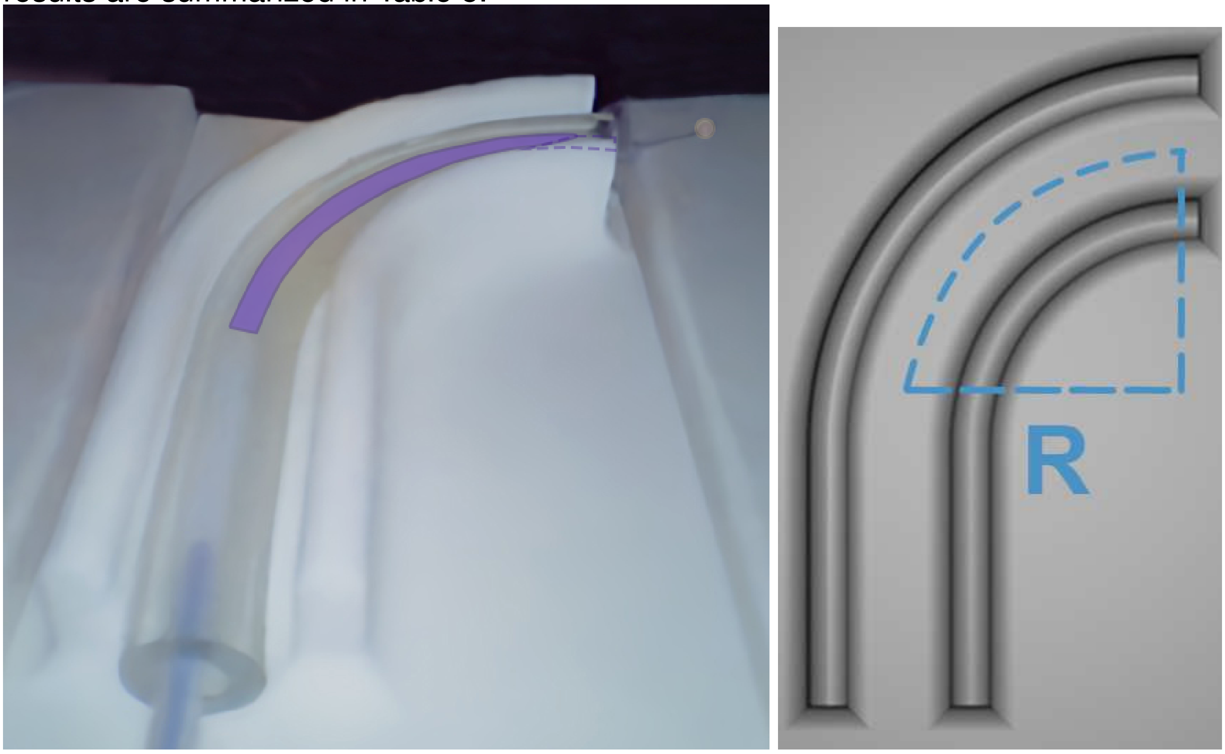

Figure 10. Overview of gradient pulling experiment where robotic guidewire is constrained within pre-curved phantoms.

(A) Real-world image of a gradient pulling experiment featuring the robot placed inside a pre-curved phantom with a 25 mm radius. To enhance visual clarity, the sleeve is highlighted in purple, and the magnetic tip is highlighted in yellow. (B) A 3D model of the phantom is provided for reference, with the curvature radius denoted as R.

Table 5. Summary of the gradient pulling behavior of the tethered magnetic tip in the robotic guidewire under varying MRI gradient strengths

		Curvature Radius, R (mm)		
		Sharp, 15	Medium, 20	Rounded, 25
Gradient Strength (%)	90	✓	✓	✓
	80	✓	✓	✓
	70	✓	✓	✓
	60	✓	✓	✓
	50	×	✓	✓
	40	×	×	✓
	30	×	×	×
	20	×	×	×
	10	×	×	×

Summary of the gradient pulling behavior of the tethered magnetic tip in the robotic guidewire

under varying MRI gradient strengths, constrained within pre-curved phantoms of different radii. 527
Successful gradient pulling is indicated by ✓, while unsuccessful attempts are marked with ×. 528

Navigation Through Confined Space

For the robotic guidewire to be effective, it must demonstrate the ability to navigate sharp corners within a confined environment. These conditions mimic the complex endoscopic pathways found in the human body, such as the aortic arch, the Circle of Willis, and bronchial bifurcations. This experiment aims to demonstrate the robot's capability to maneuver such angles.

A phantom was designed for this purpose, as shown in Figure 12(H), with the robotic guidewire positioned beside it for scale reference. The phantom was positioned horizontally in the isocentre of the MRI bore. The experiment contains a straightforward navigation task, guiding the robot along a straight path from the bottom of the phantom to the North branch (see Figure 12(B)). Then navigation into branches sequentially deviated by 45° was demonstrated, North-West branch (Figure 12(A)), West branch (Figure 12(D)), South-West branch (Figure 12(G)). The robot's ability to navigate the symmetrical set was also demonstrated, navigating into the North-East, East, and South-East branches. Each navigation was successfully performed three times to demonstrate repeatability. A comprehensive overview of the robot's navigations through all branches of the phantom is provided in Figure 12(A-D, F, G, and I) and Supplementary Video S2. Supplementary Video S1 shows a single example from these navigations (South-West pathway). Additionally, Figure 11 displays a series of MR images of the phantom embedded in an agarose gel, captured under three conditions: with no steel ball, with the 1.0 mm low carbon steel ball positioned at the entrance to the East branch, and with the ball located within the North-East branch of the phantom. This demonstrates the capacity of the MRI system to image both phantom and robot simultaneously, as seen in Figure 11(b-c).

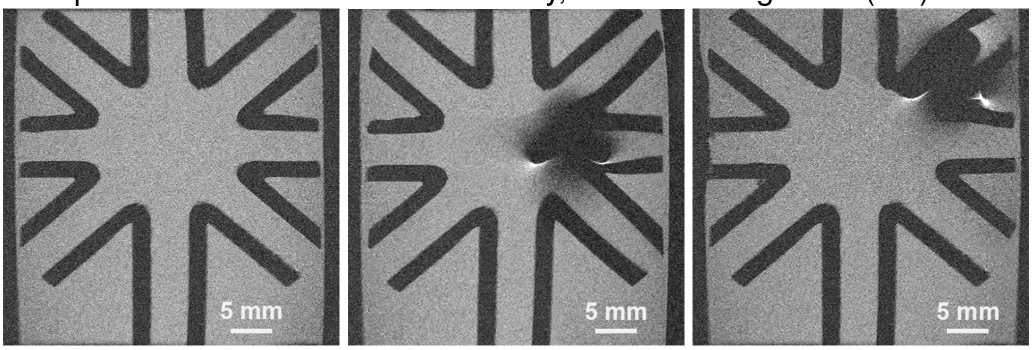

Figure 11. Set of MR images illustrating the confined-space phantom.

(A) the phantom alone, (B) with a 1 mm diameter low-carbon steel ball positioned at the entrance to the East branch, and (C) with a 1 mm diameter low-carbon steel ball located within a single navigation branch. Note, these figures were produced with the objective of demonstrating simultaneous imaging of the ball bearing and the phantom. Here the ball is not attached to its tether but embedded in the phantom with 1% agarose and 5 nM Gadolinium (Dotarem). This explains the absence of a tether from the MR Images.

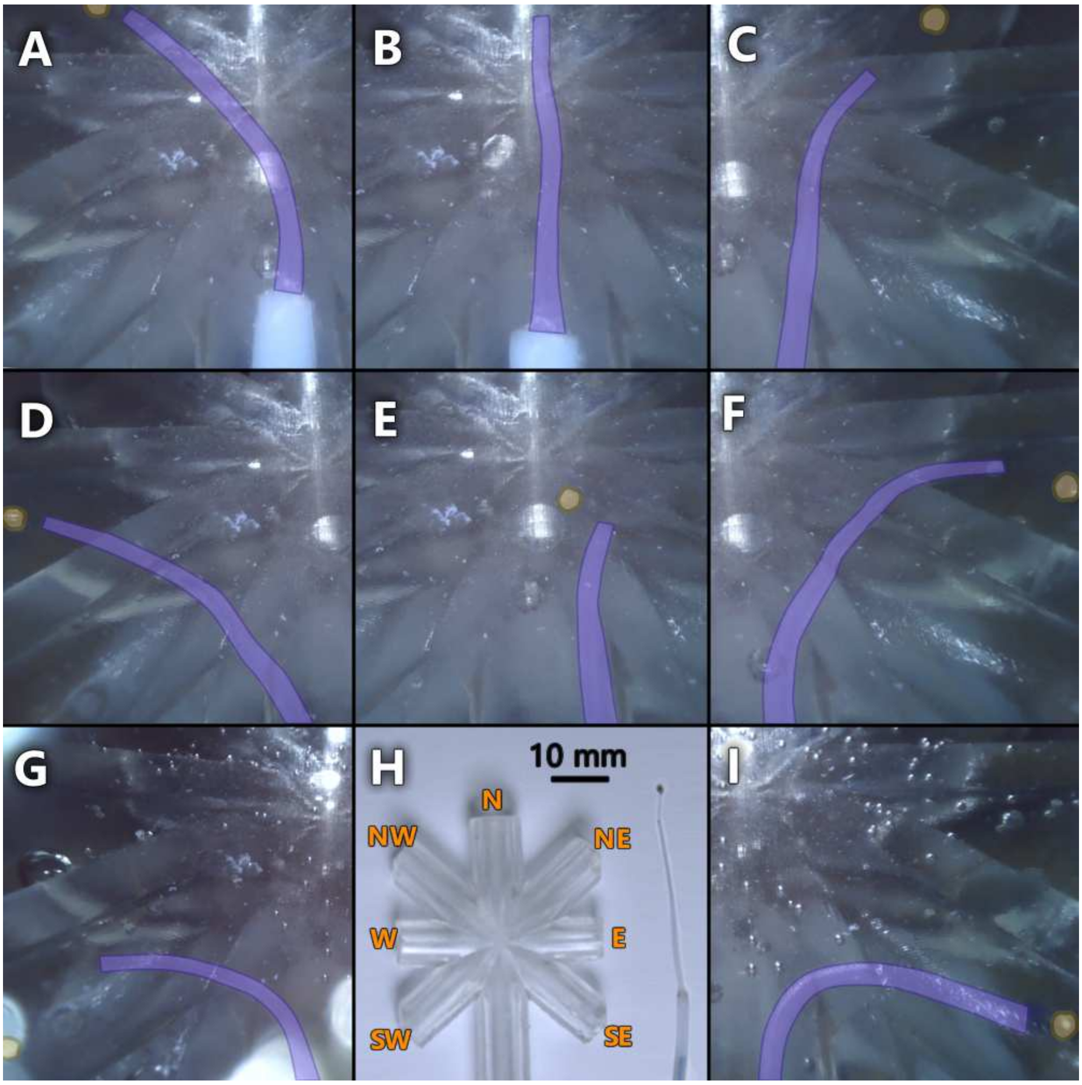

Figure 12. Overview of navigation within the confined-space phantom.

Subfigure (H) presents a real-world photo of the phantom and the robot, providing a reference for scale and branch labels used in the experiment: W for west, N for north, E for east, and intermediate directions such as NW for northwest. The central figure (E) depicts the robot positioned at the center of the phantom before selecting any specific branch. The remaining subfigures (A–D, F, G, and I) correspond to the navigations into the branches with directional labels as corresponding in subfigure (H).

Maze Navigation Experiment

To evaluate the robotic guidewire's performance, a maze-like phantom, designed to replicate the challenges encountered whilst navigating the tortuous pathways of the human anatomy, was constructed (see Figure 13). The guidewire relied on incremental leader-follower motion and magnetic gradient pulling to guide the tethered magnetic tip along the desired path, with the silicone sleeve following the same trajectory. As per the design, the robot tip advanced piecewise with the flexible sleeve stabilizing the movement, allowing for navigation through various sigmoidal curves. This experiment further confirmed the system's ability to leverage magnetic gradient pulling both tangentially and orthogonally. In total, four different routes were used in this phantom, which are shown in Supplementary Video S3. An overview of the maze navigation is shown in Figure 13(a), with corresponding MR images in Figure 13(b) and a singular example in Supplementary Video S1.

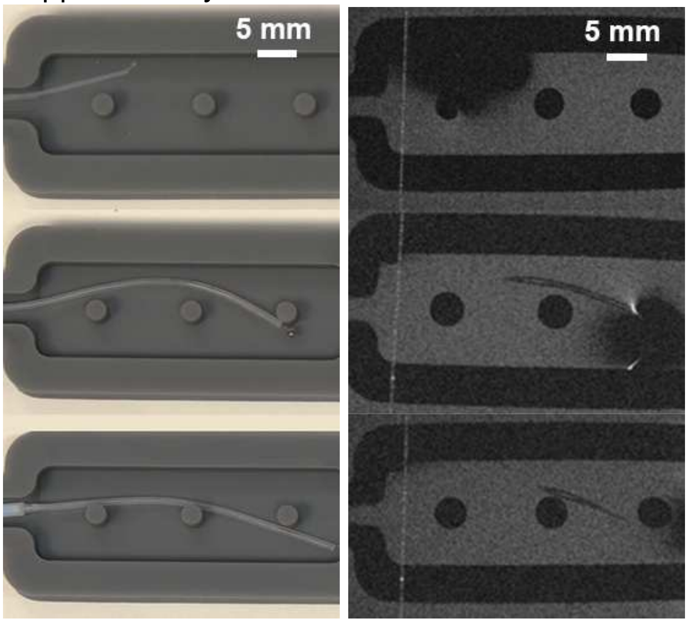

Figure 13. Overview of the maze phantom navigation.

(A) visual images of the three stages of maze phantom navigation, and (B) corresponding MR images of the maze phantom navigation stages shown in (a). The maze navigation stages are displayed in a top-to-bottom sequence, representing the start-to-end progression of the navigation. As well as the well-documented plume of signal noise, the MR Image also shows the follower sleeve, a potentially useful guide for any future work on shape reconstruction.

DISCUSSION

[R1.1] In this study, we present a new approach to gradient-pulling actuation of a soft tethered ball under MR gradients. We began by outlining the fundamental principles of MRI actuation, focusing on the key variables used to calculate the pulling forces exerted on ferrous objects by the MRI magnetic gradient. This included examining the influence of object shape on the robot's behavior and the importance of maintaining uniform symmetry to avoid the effects of an "easy-axis." A comparative analysis was conducted on the MRI signal voids produced by 1.5 mm and 1 mm chrome steel, as well as 1.5 mm and 1 mm low-carbon steel, with the magnetic response of these materials analyzed using a commercial SQUID machine. By comparing the MRI signal void against the magnetic saturation limits, we determined that 1 mm low-carbon steel was the most suitable material for gradient pulling (see Equation 4). However, testing was limited to only two materials, and further analysis of other ferrous materials is needed. The higher magnetic saturation of low-carbon steel raised the question of whether this reduction directly correlates with chrome/carbon content or follows a non-linear relationship.

We explored the feasibility of leader-follower principles by tethering the ball bearing to function as a guidewire for a flexible sleeve. A system was developed to dynamically adjust the tether length using a nitinol wire inside the inserter (PTFE tube), facilitating smooth ball movement and constraining the guidewire's shape during gradient orientation changes. This enabled a stepwise navigation strategy, as illustrated in Figure 13(a).

For the tether, medical suture was selected for its biocompatibility and low-friction properties, while a silicone sleeve was chosen for the sleeve due to its flexibility. To evaluate the resistance between the tether and the sleeve, we conducted a tribological analysis, quantifying the friction forces encountered during gradient pulling.

These findings underscore the need for further investigation into the friction forces during actuation and potential strategies to mitigate them. Additionally, we conducted experiments to assess the robotic guidewire's deformation under various configurations. By varying both the tether and sleeve lengths and examining the system's response to different MRI gradient strengths, we gained insights into the interaction between the robotic guidewire configuration and the applied MRI gradient.

The results revealed that increased sleeve length led to larger error margins in the final robot position, likely due to resonant frequency effects and interaction with the actuation signal. The deformation range initially remained limited to a few degrees under the highest 90% gradient strength for configurations with a 5 mm sleeve length. However, with longer sleeve lengths, full deformation occurred, even at the lowest 30% gradient strength. A comparison of Figures 8(c, e) indicates that configurations with additional tether resulted in a larger deformation range, likely due to the leverage provided by the extra tether. The deformation metric plots in Figure 9 show that extra tether increases the final tip inclination angle (approaching orthogonality), increases the deformation range for longer guidewire configurations, and leads to less controllable deformation, as shown by the correlation between the minimum-to-maximum deformation range and sleeve length in Figure 9(c).

We evaluated the ability of the proposed robotic guidewire design to leverage tangential gradient pulling while constrained within pre-deformed tubes of varying curvature sharpness (as seen in Figure 10). Table 5 summarizes the findings of this experiment, illustrating that pathways with sharper curvatures (i.e., smaller radius of curvature) introduce additional friction forces, thereby requiring a higher gradient magnitude to achieve successful pulling. This is important as this phenomenon can pose an upper limit on the sharpness of the curvatures that the robotic guidewire can negotiate during a real-world navigation. Therefore, additional experiments to examine this phenomenon further are planned.

Finally, we assessed the ability of the robotic guidewire to navigate sharp corners using a phantom where each branch deviated from the vertical axis by increments of 45° (Figure 12).

In conclusion, the proposed robotic guidewire design generates signal noise in MR images but not so severe that the guidewire cannot be localized. Low-carbon steel only slightly increases the signal noise area (by around 11%), as shown in Figure 2 and Table 1 whilst significantly increasing the available magnetic force (by around 42%). This ensures that the surrounding environment remains visible without obstruction (see Figures 11 and 13(b)). An interesting future study is to expand the search-space of ferrous materials to try and further optimize this signal void/pull force ratio. The magnetic pulling force exerted on the magnetic tip is sufficient to overcome frictional forces, enabling the ball to be guided to the desired location using MRI gradients, followed by the sleeve, effectively implementing leader-follower navigation. Although friction forces between the tether and sleeve are manageable, further investigation is needed to optimize this aspect. The robotic guidewire has demonstrated the ability to navigate through predefined pathways and confined spaces, showcasing its potential for full-scale navigation.

[R1.3]In this study, we utilized a 1 mm diameter magnetic sphere at the tip of the guidewire to demonstrate the feasibility of MRI gradient-based actuation. While effective for initial validation, we recognize that the current bead size imposes limitations on the range of potential intravascular applications, particularly in smaller vessels. As part of future work, we aim to miniaturize the magnetic tip via further exploration of materials - both the ferrous sphere and the interface between suture and follower sheath - to enhance compatibility with a broader range of clinical scenarios and improve the overall versatility of the system.

[R2.1] Further improvements in the imaging sequence and interpretation methods are necessary. For example, analyzing the shape of signal noise in MR images could assist in pinpointing the magnetic tip's location, thereby enhancing navigation and enabling partial automation of the procedure. Moreover, by overlaying the 1-mm-diameter spherical shape (associated with the magnetic tip) onto a previously acquired, artifact-free image—and adjusting for any anatomical shifts— it would be possible to develop a real-time MRI guidance system for surgeons. This strategy would effectively remove artifacts from the surgical view, offering a much clearer and more user-friendly navigation platform during procedures. Another point of interest is to investigate the options for a corrosion resistant coating for the low-carbon steel ball, this would clearly improve longevity and long-term performance but would also open up the fundamental design to a wider range of possible materials. The experiments were conducted on a pre-clinical MRI system, which features a strong background field $\vec{B}_0$ and field gradients. In order that clinically relevant demonstrations can increase the technological readiness level of this proof-of-concept design, additional work is required to improve robot performance in MRI systems with approximately 10x lower gradient amplitudes, enabling its compatibility with a clinical routine MRI system.

An additional area of interest pertains to interleaved actuation and imaging, which can be achieved by alternating imaging sequences (approximately 50 ms) with actuation sequences (up to 500 ms) to provide real time sensing via MR Images. The work presented here, along with the future studies mentioned, will pave the way for an autonomous, gradient-driven, self-sensing robotic guidewire platform.

Finally, this leader-follower robotic system is limited to single-point (tip) control, leaving full-shape control around complex pathways as open challenges[10,43–45]. Achieving this level of control necessitates advances in both material design and fabrication, as well as sophisticated control algorithms to navigate the complex gradient fields of the MRI system. In future work, we aim to utilize multi-point control shape-forming principles of guidewire navigation, moving beyond leader-follower principles, to achieve more flexible and continuous navigations through complex and constrained environments.

RESOURCE AVAILABILITY

Lead contact

Requests for further information and resources should be directed to and will be fulfilled by the lead contact, Nikita Murasovs (elnmur@leeds.ac.uk).

Materials availability

This study did not generate new materials.

Data and code availability

- Any additional information required to reanalyze the data reported in this paper is available from the lead contact upon request.

ACKNOWLEDGMENTS

We would like to express our gratitude to Samwise Wilson for his assistance in the selection and repair of equipment. Special thanks to Leah Khazin and Ampere Kui for their assistance with the experimental MR setup and imaging. This work was supported in part by the Engineering and Physical Sciences Research Council (EPSRC) under Grants EP/Y037235/1 and EP/V009818/1, the European Research Council (ERC) through the European Union's Horizon 2020 Research and Innovation Programme under Grant 818045, and by the National Institute for Health and Care Research (NIHR) Leeds Biomedical Research Centre (BRC) (NIHR203331). Additionally, J.E.S. acknowledges funding from the Wellcome Trust (219420/Z/19/Z) and the MRC (MR/X502789/1). Any opinions, findings, and conclusions, or recommendations expressed in this article are those of the authors and do not necessarily reflect the views of the EPSRC, the ERC, the NIHR, the Wellcome Trust, or the MRC.

AUTHOR CONTRIBUTIONS

Conceptualization, N.M. and P.L.; methodology, N.M, P.L., A.B., Y.L.M., J.A., O.C., and J.E.S.; investigation, N.M., P.L., A.B., Y.L.M., J.A., O.C., and J.E.S.; writing—original draft, N.M., P.L., and J.E.S; writing–-review & editing, N.M., P.L., J.H.C., J.E.S., and P.V.; funding acquisition, P.L, J.H.C., J.E.S., and P.V.; resources, P.L., J.A., O.C., J.E.S., and P.V.; supervision, P.L., J.E.S., and P.V.

DECLARATION OF INTERESTS

The authors declare no competing interests.

DECLARATION OF GENERATIVE AI AND AI-ASSISTED TECHNOLOGIES

During the preparation of this work, the author(s) used ChatGPT to refine the text for clarity, conciseness, and grammatical accuracy. After using this tool or service, the author(s) reviewed and edited the content as needed and take(s) full responsibility for the content of the publication.

SUPPLEMENTAL INFORMATION INDEX

Video S1. Demonstration of the actuation principle; short demo of the confined space and maze experiments.

Video S2. Demonstration of the navigation into all pathways of the confined space phantom.

Video S3. Demonstration of the navigation into all pathways of the maze phantom.

References

1. Kim, S., Laschi, C., and Trimmer, B. (2013). Soft robotics: a bioinspired evolution in robotics. Trends in biotechnology *31*, 287–294.

2. Rus, D., and Tolley, M.T. (2015). Design, fabrication and control of soft robots. Nature *521*, 467–475.

3. Cianchetti, M., Laschi, C., Menciassi, A., and Dario, P. (2018). Biomedical applications of soft robotics. Nature Reviews Materials *3*, 143–153.

4. Sitti, M., Ceylan, H., Hu, W., Giltinan, J., Turan, M., Yim, S., and Diller, E. (2015). Biomedical applications of untethered mobile milli/microrobots. Proceedings of the IEEE *103*, 205–224.

5. Wang, B., Kostarelos, K., Nelson, B.J., and Zhang, L. (2021). Trends in micro-/nanorobotics: materials development, actuation, localization, and system integration for biomedical applications. Advanced Materials *33*, 2002047.

6. Erin, O., Boyvat, M., Tiryaki, M.E., Phelan, M., and Sitti, M. (2020). Magnetic resonance imaging system–driven medical robotics. Advanced Intelligent Systems *2*, 1900110.

7. Hwang, J., Kim, B., Jin, C., Lee, G., Jeong, H., Lee, H., Noh, J., Lim, S.J., Kim, J.y., and Choi, H. (2025). Shortwave infrared imaging of a quantum dot-based magnetic guidewire toward non-fluoroscopic peripheral vascular interventions. Small *21*, 2404251.

8. Pittiglio, G., Orekhov, A.L., da Veiga, T., Calò, S., Chandler, J.H., Simaan, N., and Valdastri, P. (2023). Closed loop static control of multi-magnet soft continuum robots. IEEE Robotics and Automation Letters *8*, 3980–3987.

9. Heunis, C.M., Wotte, Y.P., Sikorski, J., Furtado, G.P., and Misra, S. (2020). The armm system-autonomous steering of magnetically-actuated catheters: Towards endovascular applications. IEEE Robotics and automation letters *5*, 705–712.

10. Pittiglio, G., Chandler, J.H., da Veiga, T., Koszowska, Z., Brockdorff, M., Lloyd, P., Barry, K.L., Harris, R.A., McLaughlan, J., Pompili, C. et al. (2023). Personalized magnetic tentacles for targeted photothermal cancer therapy in peripheral lungs. Communications Engineering *2*, 50.

11. Roesthuis, R.J., and Misra, S. (2016). Steering of multisegment continuum manipulators using rigid-link modeling and fbg-based shape sensing. IEEE transactions on robotics *32*, 372–382.

12. Moreira, P., Boskma, K.J., and Misra, S. (2017). Towards mri-guided flexible needle steering using fiber bragg grating-based tip tracking. In 2017 IEEE International Conference on Robotics and Automation (ICRA). IEEE pp. 4849–4854.

13. Pane, S., Zhang, M., Iacovacci, V., Zhang, L., and Menciassi, A. (2022). Contrast-enhanced ultrasound tracking of helical propellers with acoustic phase analysis and comparison with color doppler. APL bioengineering *6*.

14. Tiryaki, M.E., Demir, S.O., and Sitti, M. (2022). Deep learning-based 3d magnetic microrobot tracking using 2d mr images. IEEE Robotics and Automation Letters *7*, 6982–6989.

15. Diller, E., Giltinan, J., Lum, G.Z., Ye, Z., and Sitti, M. (2016). Six-degree-of-freedom magnetic actuation for wireless microrobotics. The International Journal of Robotics Research *35*, 114–128.

16. Felfoul, O., Becker, A.T., Fagogenis, G., and Dupont, P.E. (2016). Simultaneous steering and imaging of magnetic particles using mri toward delivery of therapeutics. Scientific reports *6*, 33567.

17. Lalande, V., Gosselin, F.P., and Martel, S. (2010). Experimental demonstration of a swimming robot propelled by the gradient field of a magnetic resonance imaging (mri) system. pp. 103–108.

18. Becker, A.T., Felfoul, O., and Dupont, P.E. (2015). Toward tissue penetration by mri-powered millirobots using a self-assembled gauss gun. pp. 1184–1189.

19. Latulippe, M., Felfoul, O., Dupont, P.E., and Martel, S. (2016). Enabling automated magnetic resonance imaging-based targeting assessment during dipole field navigation. Applied Physics Letters *108*.

20. Settecase, F., Sussman, M.S., Wilson, M.W., Hetts, S., Arenson, R.L., Malba, V., Bernhardt, A.F., Kucharczyk, W., and Roberts, T.P. (2007). Magnetically-assisted remote control (marc) steering of endovascular catheters for interventional mri: A model for deflection and design implications. Medical physics *34*, 3135–3142.

21. Vartholomeos, P., Bergeles, C., Qin, L., and Dupont, P.E. (2013). An mri-powered and controlled actuator technology for tetherless robotic interventions. The International Journal of Robotics Research *32*, 1536–1552.

22. Lalande, V., Gosselin, F.P., Vonthron, M., Conan, B., Tremblay, C., Beaudoin, G., Soulez, G., and Martel, S. (2015). In vivo demonstration of magnetic guidewire steerability in a mri system with additional gradient coils. Medical physics *42*, 969–976.

23. Zhang, K., Krafft, A.J., Umathum, R., Maier, F., Semmler, W., and Bock, M. (2010). Real-time mr navigation and localization of an intravascular catheter with ferromagnetic components. Magnetic Resonance Materials in Physics, Biology and Medicine *23*, 153–163.

24. Gosselin, F.P., Lalande, V., and Martel, S. (2011). Characterization of the deflections of a catheter steered using a magnetic resonance imaging system. Medical physics *38*, 4994–5002.

25. Leclerc, J., Ramakrishnan, A., Tsekos, N.V., and Becker, A.T. (2017). Magnetic hammer actuation for tissue penetration using a millirobot. IEEE Robotics and Automation Letters *3*, 403–410.

26. Erin, O., Boyvat, M., Lazovic, J., Tiryaki, M.E., and Sitti, M. (2021). Wireless mri-powered reversible orientation-locking capsule robot. Advanced Science *8*, 2100463.

27. Vartholomeos, P., Akhavan-Sharif, M.R., and Dupont, P.E. (2012). Motion planning for multiple millimeter-scale magnetic capsules in a fluid environment. pp. 1927–1932.

28. Erin, O., Gilbert, H.B., Tabak, A.F., and Sitti, M. (2019). Elevation and azimuth rotational actuation of an untethered millirobot by mri gradient coils. IEEE Transactions on Robotics *35*, 1323–1337.

29. Tuna, E.E., Liu, T., Jackson, R.C., Poirot, N.L., Russell, M., and Çavuşoğlu, M.C. (2018). Analysis of dynamic response of an mri-guided magnetically-actuated steerable catheter system. 2018 IEEE/RSJ International Conference on Intelligent Robots and Systems (IROS) pp. 1–9.

30. Abbott, J.J., Diller, E., and Petruska, A.J. (2020). Magnetic methods in robotics. Annual Review of Control, Robotics, and Autonomous Systems *3*, 57–90.

31. Lloyd, P., Onaizah, O., Pittiglio, G., Vithanage, D.K., Chandler, J.H., and Valdastri, P. (2022). Magnetic soft continuum robots with braided reinforcement. IEEE Robotics and Automation Letters *7*, 9770–9777.

32. Pittiglio, G., Lloyd, P., da Veiga, T., Onaizah, O., Pompili, C., Chandler, J.H., and Valdastri, P. (2022). Patient-specific magnetic catheters for atraumatic autonomous endoscopy. Soft robotics *9*, 1120–1133.

33. Hu, W., Lum, G.Z., Mastrangeli, M., and Sitti, M. (2018). Small-scale soft-bodied robot with multimodal locomotion. Nature *554*, 81–85.

34. Ye, Z., and Sitti, M. (2014). Dynamic trapping and two-dimensional transport of swimming microorganisms using a rotating magnetic microrobot. Lab on a Chip *14*, 2177–2182.

35. Abbott, J.J., Ergeneman, O., Kummer, M.P., Hirt, A.M., and Nelson, B.J. (2007). Modeling magnetic torque and force for controlled manipulation of soft-magnetic bodies. IEEE Transactions on Robotics *23*, 1247–1252.

36. Tiryaki, M.E., and Sitti, M. (2022). Magnetic resonance imaging-based tracking and navigation of submillimeter-scale wireless magnetic robots. Advanced Intelligent Systems *4*, 2100178.

37. AZO Materials (2022). AISI 52100 Alloy Steel (UNS G52986). . Available at `https://www.azom.com/article.aspx?ArticleID=6704` (Accessed: 2024-02-03).

38. AZO Materials (2012). AISI 1010 Carbon Steel (UNS G10100). . Available at `https://www.azom.com/article.aspx?ArticleID=6539` (Accessed: 2024-02-03).

39. De Groh III, H.C., Geng, S.M., Niedra, J.M., and Hofer, R.R. Magnetic properties of fe-49co-2v alloy and pure fe at room and elevated temperatures. Tech. Rep. The National Aeronautics and Space Administration (NASA) (2018).

40. Zhang, L., Li, W., Lin, C., and Zhou, Z. (2017). Friction behavior at the interface between surgical sutures and tissues. Tribology Letters *65*, 1–15.

41. Freudenberg Medical (2015). Helixmark catalog. . Available at `https://www.freudenbergmedical.com/ecomaXL/files/HelixMark_Catalog.pdf` (Accessed: 2024-02-03).

42. OpenCV Team (2024). Camera calibration with opencv. . Available at `https://docs.opencv.org/4.x/dc/dbb/tutorial_py_calibration.html` (Accessed: 2024-02-03).

43. Cianchetti, M., Ranzani, T., Gerboni, G., Nanayakkara, T., Althoefer, K., Dasgupta, P., and Menciassi, A. (2014). Soft robotics technologies to address shortcomings in today's minimally invasive surgery: the stiff-flop approach. Soft robotics *1*, 122–131.

44. Azizi, A., Tremblay, C.C., Gagné, K., and Martel, S. (2019). Using the fringe field of a clinical mri scanner enables robotic navigation of tethered instruments in deeper vascular regions. Science Robotics *4*, eaax7342.

45. da Veiga, T., Pittiglio, G., Brockdorff, M., Chandler, J.H., and Valdastri, P. (2023). Six-degree-of-freedom localization under multiple permanent magnets actuation. IEEE Robotics and Automation Letters *8*, 3422–3429.

All Cell Press **life and medical science** journals, and the multidisciplinary journal **iScience**, use the **STAR Methods** format for reporting materials and methods. Other Cell Press journals use a non-structured **methods** format; for those journals, please **delete** the contents of this page from the template and refer instead to the **methods** template on page 3.

If you are publishing in a STAR Methods journal, please refer to the appropriate guide for authors:

- *Cell* authors should download the guide for *Cell* authors available here
- All other journal authors should use this version of the guide

STAR METHODS

Key resources table

To create the KRT, please use the KRT webform or the Word template and upload this file separately.

Experimental model and study participant details

Method details

Quantification and statistical analysis

Additional resources

Cell.com homepage: https://www.cell.com
Templates for Cell Press authors: https://www.cell.com/article-templates